

Anatomy of the tsunami and Lamb waves-induced ionospheric signatures generated by the 2022 Hunga Tonga volcanic eruption

E. Munaibari¹, L. Rolland¹, A. Sladen¹, B. Delouis¹

1 – Université Côte d'Azur, Observatoire de la Côte d'Azur, CNRS, IRD, Géoazur, 250 rue Albert Einstein, Sophia Antipolis 06560 Valbonne, France, edhah.munaibari@geoazur.unice.fr

Key points:

- The tsunami of the 2022 Hunga Tonga-Hunga Ha'apai volcanic eruption triggered ionospheric imprints across the Pacific Ocean
- The eruption produces high ionospheric noise, especially in the near field, making its tsunami ionospheric imprints harder to identify
- The ionospheric imprints of the eruption-triggered Lamb wave are consistent with internal gravity waves origin

Abstract

As tsunamis propagate across open oceans, they remain largely unseen due to the lack of adequate sensors, hence limiting the scope of existing tsunami warnings. A potential alternative method relies on the Global Navigation Satellites Systems to monitor the ionosphere for Traveling Ionospheric Disturbances created by tsunami-induced internal gravity waves (IGWs). The approach has been applied to tsunamis generated by earthquakes but rarely by undersea volcanic eruptions injecting energy into both the ocean and the atmosphere. The large 2022 Hunga Tonga-Hunga Ha'apai volcanic eruption tsunami is thus a challenge for tsunami ionospheric imprint detection. Here, we show that in near-field regions (<1500km), despite the complex wavefield, we can isolate the tsunami imprint. We also highlight that the eruption-generated Lamb wave's ionospheric imprints show an arrival time and an amplitude spatial pattern consistent with internal gravity wave origin.

Plain Language Summary

To complement conventional tsunami warning systems, it is possible to rely on the imprint of the tsunami in the ionosphere, a high-altitude layer of the atmosphere. This imprint can be tracked using the Global Navigation Satellites Systems to measure the Total Electron Content (TEC) of the ionosphere. On Jan. 15, 2022, the submarine volcano of Hunga Tonga-Hunga Ha'apai erupted, providing a unique opportunity to test the approach on a tsunami generated by a volcanic eruption. Here, we study the tsunami's ionosphere response, the pressure pulse the eruption generated, and the underlying physical mechanisms. We find that the eruption caused a particularly high ionosphere activity in the near-field region, making the tsunami signature assessment and use for early-warning more challenging but still possible.

45 **1. Introduction**

46 Tsunamis are natural hazards that have already claimed the lives of more than 250000
47 civilians globally (Mizutori & Guha-Sapir, 2018). Tsunamis are commonly monitored on shores by
48 coastal tide gauges or in deep oceans by tsunami buoys. These instruments provide direct
49 measurements of the tsunami but can be insufficient for early warnings because (1) tide gauges
50 are located on the coasts, giving little to no time for a warning, and (2) tsunami buoys are
51 expensive to deploy and maintain, resulting in a limited sampling of the oceans, not sufficient for
52 near-field warning. An alternative but indirect method centers around the computation of the
53 ionospheric total electron content (TEC) to track tsunami propagation. The first tsunami-induced
54 ionospheric (TEC) signature was presented by Artru et al. (2005), and since, this technique has
55 been used to identify and characterize the TEC signatures of a variety of tsunamis, all initiated by
56 submarine earthquakes (Liu et al., 2006; Rolland et al., 2010; Galvan et al., 2011; Grawe & Makela,
57 2015, 2017). Underwater volcanic eruptions and landslides can also trigger tsunamis, except that
58 there haven't been many large instances in the last decades to study them in the light of modern
59 instrumentation. The 2022 explosion of the Hunga Tonga-Hunga Ha'apai (HTHH) submarine
60 volcano provides a unique opportunity to fill this gap and characterize the generated ionospheric
61 perturbations.

62 According to the US Geological Survey (USGS), the HTHH volcano (20.546°S 175.39°W ; Fig.
63 1a) violently erupted on Jan. 15, 2022, at 4:14:45 UTC (17:14:45 LT). The eruption released a
64 massive ash plume that reached an altitude of ~ 55 km (Smart 2022). It also generated a highly-
65 energetic atmospheric Lamb wave observed globally (for a few days after the eruption) in
66 different types of measurements (e.g., barometers, infrasound sensors, satellites images,
67 ionospheric measurements) (Matoza et al., 2022; Wright et al., 2022). According to Themens et al.
68 (2022), large and medium-scale traveling ionospheric disturbances (TIDs) appeared in global TEC
69 measurements following the eruption, with travel speeds ranging from 200 to 1000 m/s. They
70 attributed the two TIDs types to the initial acoustic response of the explosive eruption and the
71 energetic Lamb wave, respectively. The same findings were reported by Lin et al. (2022). In
72 addition, Astafyeva et al. (2022) used the nearfield TEC measurements to identify the presence of
73 several volcanic explosions during the event timeline. Moreover, the eruption triggered air-sea
74 (tsunami-like) waves induced by the Lamb-wave-sea coupling and observed worldwide (Kubota et
75 al., 2022; Omira et al., 2022). According to Matoza et al. (2022), the Lamb wave signature appears
76 to be consistent (arrival time, waveform) in both the ionospheric and sea-level observations.

77 The eruption also produced a classical tsunami, i.e., from direct water mass displacement,
78 detected across the Pacific Ocean (Carvajal et al., 2022), causing four casualties in Tonga (Latu,
79 2022) and two in Peru (Parra, 2022). The exact mechanism triggering the tsunami is not well-
80 understood yet, but preliminary analysis suggests a combination of submarine explosion and
81 caldera collapse (Hu et al., 2022 and reference therein). An ionospheric imprint of this tsunami
82 was reported by Matoza et al. (2022) at near-field. Here, we strengthen the study with a spatial
83 pattern analysis and expand the investigated dataset more globally (Pacific-wide). We seek to
84 isolate the ionospheric signature of the tsunami from the acoustic and Lamb signals. Because of
85 these multiple, partially overlapping signals, we don't expect the discrimination to be
86 straightforward, yet, it is a necessary step to assess the potential of TEC data for tsunami early-
87 warning even in the case of a volcanic eruption.

88 To support our TEC signal analysis, we first analyze the ionospheric imprint of a tsunami
89 initiated by the Mw 8.1 Kermadec earthquake, which occurred a year before, on March 4th, 2021
90 about 1000 km South of Tonga (29.723°S 177.279°W, based on the USGS report) (Fig. 1a). Both
91 events occurred in the Eastern region of Polynesia islands sparsely equipped with GNSS stations
92 installed onland. The size of the tsunami triggered by the Kermadec earthquake was smaller than
93 the one triggered by the HTHH event by less than one order of magnitude (respectively 3 and 20
94 cm in the near-field after Romano et al., 2021 and Lynett et al., 2022). We thus use the Kermadec
95 ionospheric imprints as a test case to help decipher the HTHH imprints in the ionosphere with a
96 sparse multi-GNSS network.

97 In addition to presenting the ionospheric imprints of the two tsunamis, we investigate how
98 the tsunami generation mechanism (earthquake vs. volcano) affects the detection of such
99 imprints. We compare the tsunami sea-level variations to the ionosphere imprints to confirm the
100 tsunami origin of the detected ionospheric imprints. Finally, we examine the ionospheric response
101 of the Lamb wave the HTHH eruption produced and compare it to that of the tsunami.
102

103 **2. Data and methods**

104 The previous detections of tsunami-induced ionospheric imprints in the literature are
105 based on the use of dense networks of GNSS receivers (Grawe & Makela, 2017 and references
106 therein). Here, the sparsity of GNSS receivers in the south Pacific area requires a single receiver
107 approach to identify the tsunami's ionospheric response and study its evolution at various
108 distances and directions. To test the single receiver technique, we examine the Kermadec tsunami
109 through the GNSS receiver located in Niue Island (NIUM; Fig. 1a), ~1400 km from the epicenter.
110 Such distance favors the detection of both the earthquake and the tsunami ionospheric signatures
111 (Fig. 1a). While the coseismic acoustic gravity wave (AGW) can be observed next to the source, the
112 ionospheric imprint of the IGW triggered by the tsunami cannot appear closer than 500 km from
113 the source and sooner than 1h after the initiation because the atmospheric wave also needs to
114 propagate vertically at a speed below 100 m/s (Occhipinti et al., 2013). For tsunami early-warning,
115 these properties make the AGW measurements more suited in the near-field (Zedek et al., 2021)
116 and the tsunami-induced IGW measurements more suited in the medium and far-field (this study).

117 From the NIUM GNSS observation data, we compute the raw slant total electron content
118 (sTEC) and apply a sequence of filters (polynomial detrend, apodization, and band-pass filter; see
119 S1 & S2 in SM for a detailed description). The bottom panel of Figure 2a depicts the raw sTEC
120 observed by the satellite-receiver pair G12-NIUM. The top x-axis in the panel indicates the satellite
121 elevation where we applied a mask removing data below 20° elevation (unlike the 10° mask
122 adopted for the rest of this work) to minimize the possible artifacts enhanced by the low elevation
123 (see G12 in Figure 3a). After that, we use the theoretical tsunami travel times (TTT) to estimate
124 the expected tsunami arrival time at a particular location (e.g., sTEC data IPPs location: the
125 intersection of the line of sight with the ionosphere shell at a certain altitude [Davies & Hartmann,
126 1997], 300km in this study), knowing that the associated TEC signature should appear
127 approximately around the same time (Rolland et al., 2010). These processing steps allow us to
128 observe two distinct signatures: the earthquake acoustic response (A1) appearing ~10 min after
129 the initiation time (IT) and the tsunami (T1) emerging within the expected arrival time. This
130 pattern is consistent over the different satellites seen by the receiver (Fig. 3a). The spatial pattern

131 of the imprints' maximum TEC amplitude around the receiver further assesses the detection.
132 According to Grawe & Makela (2015), the TEC amplitude of tsunami-induced IGWs increases from
133 upstream to downstream the receiver (Fig. 3c). The technique's applicability is made possible
134 thanks to multi-GNSS observations with an efficient azimuthal coverage that increases the
135 reliability of the detection.

136 We follow the same procedure for the HTHH tsunami, selecting GNSS receivers located in
137 several Pacific islands (Fig. 1a; Table S3 in SM), to extend our analysis with more global coverage.
138 The detection made by each receiver is independent of the others. We selected receivers with
139 multi-GNSS capability. The chosen receivers fall in a distance ranging from 700 km to 10 000 km,
140 and thus from near to far field, with respect to the tsunami source. This allows us to track the
141 fully-developed tsunami in the ionosphere as it travels across the Pacific.

142

143 **3. Results**

144 **1. Tsunami-induced TEC signatures across the Pacific Ocean**

145 We identified the ionospheric imprints of the HTHH tsunami in the TEC data from 12
146 receivers around the Pacific (Fig. 1b). The tsunami-induced ionospheric imprints are corroborated
147 by observations from other satellites for each receiver (Fig. S5 to S15 in SM). The tsunami TEC
148 amplitude and the local tsunami arrival time of the twelve series are illustrated in Table S3 of the
149 SM. These results agree with the dense-network-based study of Ravanelli et al., in review GRL,
150 2022 (specifically in the vicinity of New Caledonia and New Zealand).

151 Applying our detection method with the GNSS receiver located on Lord Howe Island (LORD;
152 Fig. 1a) during the generation and passage of the HTHH tsunami, we successfully identified its
153 ionospheric signatures, as confirmed by the two-step verification procedure (Fig. 3b,d). By
154 comparing the Kermadec and HTHH signatures (Fig. 2a,b), we see how exceptional the HTHH
155 event is; a complex time series with imprints of multiple types of waves, and an amplitude one
156 order of magnitude larger (Table S3 in SM).

157

158 **2. Ionospheric imprints comparison (earthquake-induced vs. volcanic eruption- 159 induced)**

160 To investigate the impact of the trigger source (earthquake vs. volcanic eruption) on the
161 induced ionospheric signatures of a tsunami, we focus on two TEC measurements with optimal
162 configuration (the orientation of the tsunami aligns with the local geomagnetic field, and the
163 observing geometry is downstream the receivers; Grawe & Makela, 2015): G12-NIUM (Kermadec;
164 Fig. 2a) and C01-TUVA (HTHH; Fig. 2b). Both are located in the medium field (~1400 km) and are
165 band-pass filtered from 0.7 to 10 mHz.

166 For the Kermadec event, we observe two remarkable signatures that we link to the event.
167 The first signature is the earthquake acoustic response appearing several minutes after the initiation
168 as an N-shape pulse, as routinely observed after earthquakes. We have strong arguments
169 supporting that the second signature is that of the tsunami: (1) it occurs within the expected arrival
170 time of the tsunami, (2) it has an oscillatory signature with a clear frequency peak at 1.2 mHz, in the
171 range of what is expected for the tsunami waves, (3) it is supported by the different satellites seen
172 by the receiver (Fig. 3a), and (4) the IGWs behavior of the detected signatures' maximum TEC
173 amplitude (Fig. 3c).

174 Unlike the Kermadec submarine earthquake, the HTHH submarine volcanic eruption
175 ionospheric imprints are more complex and present a richer spectrum. Besides the tsunami
176 response (T1) and the signature of the initial acoustic response (A1), a Lamb wave (L1) is visible in
177 the volcano eruption data. The two types of imprints (excluding the tsunami's) are reported by
178 Wright et al. (2022). The imprint of the tsunami emerges at the expected arrival time with an
179 amplitude of 0.58 TECU. In contrast to the earthquake case, the ionosphere during the eruption
180 experiences higher noise related to the main, massive, explosion of the eruption, and the numerous
181 different types of waves it injected into the Earth's atmosphere (Wright et al., 2022). Such noise can
182 also be seen in some of the sTEC series shown in Figure 1 (see also Fig. 3b), especially those close to
183 the volcano.

184

185 **3. Ionosphere vs. sea-level measurements**

186 To further assess the tsunami origin of the identified imprints, we compared the sTEC
187 disturbance measured offshore Galapagos Islands with the sea-level anomaly registered by a deep-
188 sea DART buoy #32413 about 800 km southwest of the Islands (Fig. 1a). Both signals have similar
189 waveforms with a peak frequency around 1.2 mHz (Fig. 4a). The emergence of the signal 30 minutes
190 earlier in the ionosphere suggests that the shoaling of the bathymetry around the Galapagos
191 archipelago slowed down the tsunami in the sea surface while allowing its induced IGWs to advance
192 ahead of it. A similar effect was observed for the 2011 Tohoku tsunami when it approached Hawaii
193 (Occhipinti et al., 2011).

194 We also note the presence of an ionospheric signature having an amplitude and a spectral
195 content similar to the tsunami imprint but 2 hours earlier (Fig. 4a). It appears to travel with a speed
196 of ~ 235 m/s and could be the imprint of an IGW triggered by the eruption and traveling all the way
197 in the atmosphere.

198

199 **4. Ionospheric imprints of the Lamb wave**

200 When examining the ionospheric (TEC) data as we search for the HTHH tsunami imprints,
201 we first notice the peculiar signature of the Lamb wave, whose raw sTEC measurements display
202 massive decreases and increases that resemble a large W-shape (Fig. S16 in SM). The Lamb wave
203 processed imprints exhibit close similarity to the tsunami's. We note that the ionospheric
204 signature of both the Lamb and the tsunami waves peak at a similar frequency of 1.2 mHz (Fig.
205 2b), with the Lamb wave displaying a more impulsive behavior. Furthermore, Figure 2e shows that
206 the Lamb wave's imprint' maximum sTEC amplitude spatial pattern exhibits IGW behavior (similar
207 to the tsunamis cases in Figures 2c and 2d), where the maximum amplitude is larger downstream
208 of the GNSS receiver. Overall, the Lamb wave signature has a larger amplitude than the tsunami
209 signature.

210 We also investigated the co-located measurements of a DART buoy's Lamb wave pressure
211 signature and its ionospheric signature in southern New Zealand (Fig. 4b). They both show an
212 impulsive waveform (in the time domain) and a broadband frequency content (Fig. 4b). In
213 addition, when corrected for traveled distances, the imprints show no delay between the arrival at
214 the buoy's location and the ionosphere and are consistent with the Lamb wave constant speed
215 (318m/s). The amplitude pattern and absence of time delay suggest that in the same way as the

216 tsunami, the Lamb wave triggered internal gravity waves (IGW), which traveled upward to
217 ionospheric heights with the same horizontal speed as the Lamb wave.

218

219 **4. Discussion**

220 The global overview of the ionospheric imprint amplitude shows interesting features (Fig.
221 1). The tsunami's smallest sTEC amplitude is observed in Hawaii. Three possible reasons could
222 have caused the lower amplitude aside from the tsunami open-ocean size itself (~6 cm zero to
223 crust recorded by the 51407 DART buoy): (1) the local time of the tsunami arrival was around 1 am
224 (Table S3), meaning a low ionization rate (compared to the daytime) and consequently a smaller
225 amplitude of detected signatures (Grawe & Makela, 2015), (2) the inefficient coupling between
226 the tsunami-induced IGWs and the local geomagnetic field, or (3) the destructive interaction
227 between the conjugate Traveling Ionospheric Disturbances (TIDs) and the direct TIDs traveling
228 away from the volcano as suggested by Themens et al. (2022). This later scenario is based on the
229 fact that Hawaii is very close to the volcano's geomagnetic conjugate point. Lin et al. (2022) also
230 reported the presence of conjugate TIDs, lending more support to this explanation.

231 In contrast, the tsunami ionospheric signature with the largest amplitude in the vicinity of
232 the Galapagos Islands suggests a tsunami with a higher open-ocean wave (~6 cm zero to crust
233 recorded by the 32413 DART buoy), which contradicts the expected wave height decay with
234 increasing distance from the source (~2 cm; model) (Ward 2002). Unlike the other identified
235 imprints, the detection near the Galapagos took place around noon local time (Table S3 in SM),
236 which contributes to the larger amplitude of the detected ionospheric imprints.

237 The lack of delay between the arrival of the Lamb wave imprints in the ionosphere and on
238 the surface, as illustrated by Figure 4b, suggests that the propagation of the Lamb acts like a
239 moving source (similar to a tsunami), forcing IGWs that travels obliquely upward (Lin et al., 2022).
240 The IGW behavior experienced by the imprints' max sTEC amplitude (depicted in Figure 3e)
241 supports such a hypothesis.

242

243 **5. Conclusions**

244 The ionospheric imprints of the tsunami generated by Jan. 15, 2022, Hunga Tonga-Hunga
245 Ha'apai volcanic eruption, as it propagates across the Pacific Ocean, are presented and investigated
246 along with that of the Mar. 4, 2021, 8.1 Mw Kermadec Islands earthquake tsunami. Our results
247 indicate that, like the ionospheric imprints of earthquake-initiated tsunamis, the imprints of the
248 tsunami generated by the HTHH eruption can be identified and isolated in the ionospheric data,
249 even with a single station approach. This result was achieved despite a high level of ionospheric
250 noise, especially in near-field, produced by the volcanic eruption. This noise complexifies the
251 detection of tsunami-induced ionospheric imprints, calling for further improvement in the filtering
252 algorithms and differentiation criteria in order to meet the high detection confidence required for
253 early warnings. Yet, the comparison with open-ocean sea-level measurements confirmed that the
254 isolated imprints were those of the tsunami.

255 Our joint analysis of the ionospheric signatures of the Lamb (pressure) and tsunami waves
256 shows that they both trigger internal gravity waves that can be distinguished thanks to their
257 different traveling speeds. Detecting the HTHH tsunami's ionospheric imprints across the Pacific
258 Ocean demonstrates the potential of our single-receiver approach. Its current implementation

259 requires a visual inspection to validate the identified imprints. This absence of automation presents
260 a limitation that we intend to overcome in future work along with utilizing detected tsunami-
261 induced ionospheric signatures to estimate the open-ocean tsunami's wave height, which is the
262 quantity of interest to tsunami early warning systems.

263
264

265 **Data and Resources**

266 All GNSS data are freely available from the Geoscience Australia data archives
267 (<ftp://ftp.data.gnss.ga.gov.au/daily/>) and the CDDIS data archives
268 (https://cddis.nasa.gov/Data_and_Derived_Products/GNSS/daily_30second_data.html). The ocean
269 bathymetry data ETOPO1 (1-minute global relief model; Amante and Eakins 2009) and the open-
270 ocean sea-level measurements (DART) are from the NOAA data archives
271 (<https://www.ngdc.noaa.gov/mgg/bathymetry/relief.html>;
272 <https://www.ngdc.noaa.gov/hazard/DARTData.shtml>). The coastal sea-level measurements (tide
273 gauge) are publicly available via the Intergovernmental Oceanographic Commission of UNESCO
274 (<http://www.ioc-sealevelmonitoring.org/>). To generate the tsunami travel times, we take
275 advantage of Geoware TTT SDK software (Wessel, 2009).

276
277

277 **Acknowledgement**

278 This work was supported by French Agence Nationale de la Recherche (ANR) under reference ANR-
279 19-CE04-0003 and Centre national d'études spatiales (CNES) for APR project UVTECGEOX. We thank
280 E. Astafyeva, P. Coisson, B. Maletckii, F. Manta, D. Mikesell & M. Ravanelli for fruitful discussions
281 within an ad-hoc Geoazur-IPGP-NGI working group on the 2022 Hunga volcano eruption.

282

283 **References**

- 284 Amante, C., & Eakins, B.W. (2009). ETOPO1 1 Arc-Minute Global Relief Model: Procedures, Data
285 Sources and Analysis. National Geophysical Data Center, NOAA.
286 <https://doi.org/10.7289/V5C8276M>
- 287 Artru, J., Ducic, V., Kanamori, H., Lognonné, P., & Murakami, M. (2005). Ionospheric detection of
288 gravity waves induced by tsunamis. *Geophys. J. Int.*, 160, 840–848.
289 <https://doi.org/10.1111/j.1365-246X.2005.02552.x>
- 290 Astafyeva, E., Maletckii, B., Mikesell, T. D., Munaibari, E., Ravanelli, M., Coisson, P., Manta, F., &
291 Rolland, L. (2022). The 15 January 2022 Hunga Tonga Eruption History as Inferred From
292 Ionospheric Observations. *Geophysical Research Letters*, 49(10).
293 <https://doi.org/10.1029/2022GL098827>
- 294 Carvajal, M., Sepúlveda, I., Gubler, A., & Garreaud, R. (2022). Worldwide Signature of the 2022
295 Tonga Volcanic Tsunami. *Geophysical Research Letters*, 49(6), 8–11.
296 <https://doi.org/10.1029/2022gl098153>
- 297 Davies, K., & Hartmann, G. K. (1997). Studying the ionosphere with the Global Positioning System.
298 *Radio Science*, 32(4), 1695–1703. <https://doi.org/10.1029/97RS00451>
- 299 Galvan, D. A., Komjathy, A., Hickey, M. P., & Mannucci, A. J. (2011). The 2009 Samoa and 2010 Chile
300 tsunamis as observed in the ionosphere using GPS total electron content. *Journal of*
301 *Geophysical Research: Space Physics*, 116(A6), n/a-n/a. <https://doi.org/10.1029/2010JA016204>

302 Grawe, M. A., & Makela, J. J. (2015). The ionospheric responses to the 2011 Tohoku, 2012 Haida
303 Gwaii, and 2010 Chile tsunamis: Effects of tsunami orientation and observation geometry. *Earth
304 and Space Science*, 2(11), 472–483. <https://doi.org/10.1002/2015EA000132>

305 Grawe, M. A., & Makela, J. J. (2017). Observation of tsunami-generated ionospheric signatures over
306 Hawaii caused by the 16 September 2015 Illapel earthquake. *Journal of Geophysical Research:
307 Space Physics*, 122(1), 1128–1136. <https://doi.org/10.1002/2016JA023228>

308 Hu, G., Li, L., Ren, Z., and Zhang, K.: The characteristics of the 2022 Tonga volcanic tsunami in the
309 Pacific Ocean, *Nat. Hazards Earth Syst. Sci. Discuss.* [preprint], [https://doi.org/10.5194/nhess-
310 2022-200](https://doi.org/10.5194/nhess-2022-200), in review, 2022.

311 Kubota, T., Saito, T., & Nishida, K. (2022). Global fast-traveling tsunamis driven by atmospheric Lamb
312 waves on the 2022 Tonga eruption. *Science*. <https://doi.org/10.1126/science.abo4364>

313 Latu, K. (2022). Prime Minister defends Deputy’s ‘no sirens’ reply as tsunami death toll rises to four.
314 Kaniva Tonga Media. [https://www.kanivatonga.nz/2022/01/prime-minister-defends-deputy-
315 no-sirens-reply-as-tsunami-death-toll-rises-to-four/](https://www.kanivatonga.nz/2022/01/prime-minister-defends-deputy-no-sirens-reply-as-tsunami-death-toll-rises-to-four/)

316 Lin, J., Rajesh, P. K., Lin, C. C. H., Chou, M., Liu, J., Yue, J., Hsiao, T., Tsai, H., Chao, H., & Kung, M.
317 (2022). Rapid Conjugate Appearance of the Giant Ionospheric Lamb Wave Signatures in the
318 Northern Hemisphere After Hunga-Tonga Volcano Eruptions. *Geophysical Research Letters*,
319 49(8). <https://doi.org/10.1029/2022GL098222>

320 Liu, J. Y., Tsai, H. F., & Jung, T. K. (1996). Total Electron Content Obtained by Using the Global
321 Positioning System. *Terrestrial, Atmospheric and Oceanic Sciences*, 7(1), 107.
322 [https://doi.org/10.3319/TAO.1996.7.1.107\(A\)](https://doi.org/10.3319/TAO.1996.7.1.107(A))

323 Lynett, P., McCann, M., Zhou, Z., Renteria, W., Borrero, J., Greer, D., Fa’anunu, O., Bosserelle, C.,
324 Jaffe, B., Selle, S. La, Ritchie, A., Snyder, A., Nasr, B., Bott, J., Graehl, N., Synolakis, C., Ebrahimi,
325 B., & Cinar, G. E. (2022). Diverse Tsunamigenesis Triggered by the Hunga Tonga-Hunga Ha’apai
326 Eruption. *Nature*, 1–22. <https://doi.org/10.1038/s41586-022-05170-6>

327 Matoza, R. S., Fee, D., Assink, J. D., Iezzi, A. M., Green, D. N., Kim, K., Toney, L., Lecocq, T.,
328 Krishnamoorthy, S., Lalande, J.-M., Nishida, K., Gee, K. L., Haney, M. M., Ortiz, H. D., Brissaud,
329 Q., Martire, L., Rolland, L., Vergados, P., Nippres, A., ... Wilson, D. C. (2022). Atmospheric waves
330 and global seismoacoustic observations of the January 2022 Hunga eruption, Tonga. *Science*.
331 <https://doi.org/10.1126/science.abo7063>

332 Mizutori, M., & Guha-Sapir, D. (2018). Economic Losses, Poverty & DISASTERS 1998-2017. Centre
333 for Research on the Epidemiology of Disasters & United Nations Office for Disaster Risk
334 Reduction. Retrieved from
335 https://www.preventionweb.net/files/61119_credeconomiclosses.pdf

336 Occhipinti, G., Coisson, P., Makela, J. J., Allgeyer, S., Kherani, A., Hébert, H., & Lognonné, P. (2011).
337 Three-dimensional numerical modeling of tsunami-related internal gravity waves in the
338 Hawaiian atmosphere. *Earth, Planets and Space*, 63(7), 847–851.
339 <https://doi.org/10.5047/eps.2011.06.051>

340 Occhipinti, G., Rolland, L., Lognonné, P., & Watada, S. (2013). From Sumatra 2004 to Tohoku-Oki
341 2011: The systematic GPS detection of the ionospheric signature induced by tsunamigenic
342 earthquakes. *Journal of Geophysical Research: Space Physics*, 118(6), 3626–3636.
343 <https://doi.org/10.1002/jgra.50322>

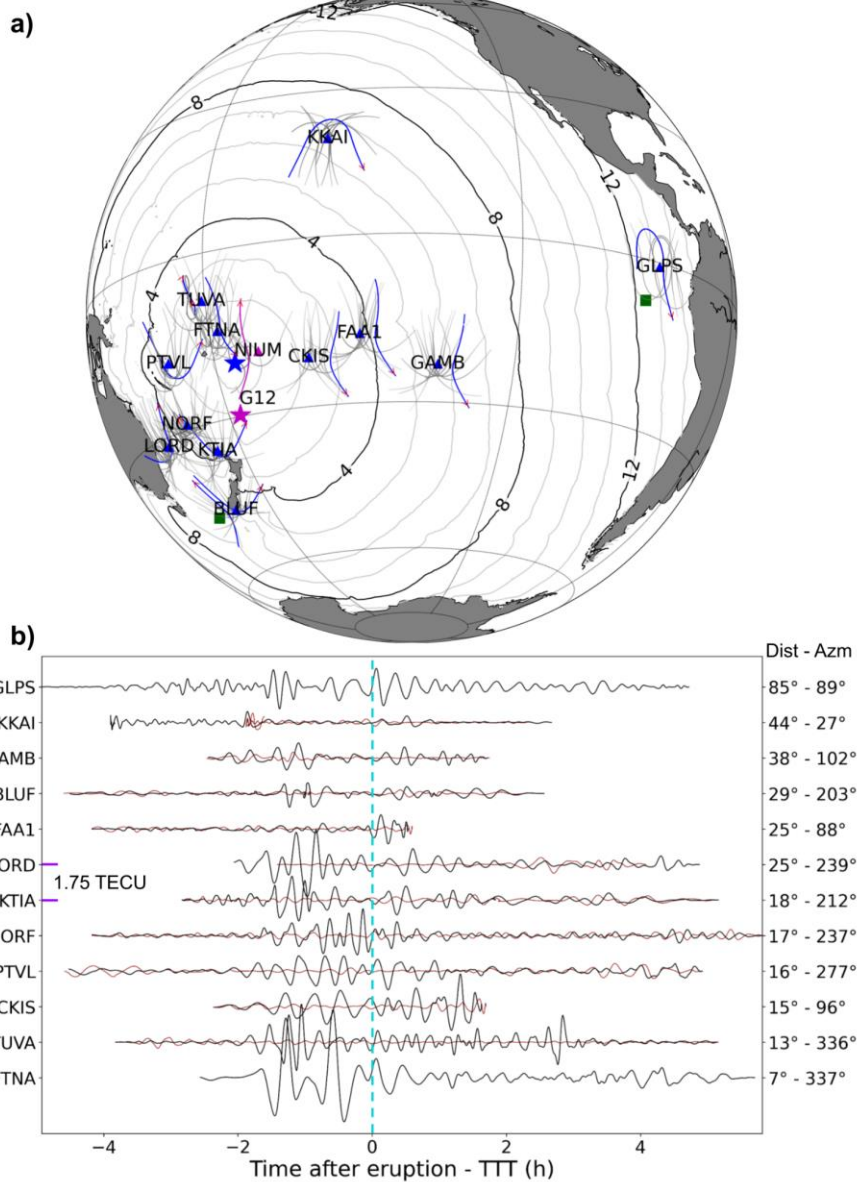
- 344 Omira, R., Ramalho, R.S., Kim, J. et al. Global Tonga tsunami explained by a fast-moving atmospheric
345 source. *Nature* (2022). <https://doi.org/10.1038/s41586-022-04926-4>
- 346 Parra, N. (2022). Two deaths and tsunami damage reported in Peru: country did not issue an alert.
347 *Radio Bío-Bío*. [https://www.biobiochile.cl/noticias/internacional/america-](https://www.biobiochile.cl/noticias/internacional/america-latina/2022/01/15/reportan-dos-muertes-y-danos-por-tsunami-en-peru-pais-no-emitio-alerta.shtml)
348 [latina/2022/01/15/reportan-dos-muertes-y-danos-por-tsunami-en-peru-pais-no-emitio-](https://www.biobiochile.cl/noticias/internacional/america-latina/2022/01/15/reportan-dos-muertes-y-danos-por-tsunami-en-peru-pais-no-emitio-alerta.shtml)
349 [alerta.shtml](https://www.biobiochile.cl/noticias/internacional/america-latina/2022/01/15/reportan-dos-muertes-y-danos-por-tsunami-en-peru-pais-no-emitio-alerta.shtml)
- 350 Rolland, L. M., Occhipinti, G., Lognonné, P., & Loevenbruck, A. (2010). Ionospheric gravity waves
351 detected offshore Hawaii after tsunamis. *Geophysical Research Letters*, 37(17).
352 <https://doi.org/10.1029/2010GL044479>
- 353 Romano, F., Gusman, A. R., Power, W., Piatanesi, A., Volpe, M., Scala, A., & Lorito, S. (2021). Tsunami
354 Source of the 2021 M W 8.1 Raoul Island Earthquake From DART and Tide-Gauge Data Inversion
355 . *Geophysical Research Letters*, 48(17), 1–11. <https://doi.org/10.1029/2021gl094449>
- 356 Smart, D. (2022). The first hour of the paroxysmal phase of the 2022 Hunga Tonga Hunga Ha’apai
357 volcanic eruption as seen by a geostationary meteorological satellite. *Weather*, 77(3), 81–82.
358 <https://doi.org/10.1002/wea.4173>
- 359 Themens, D. R., Watson, C., Žagar, N., Vasylykevych, S., Elvidge, S., McCaffrey, A., et al. (2022). Global
360 propagation of ionospheric disturbances associated with the 2022 Tonga Volcanic Eruption.
361 *Geophysical Research Letters*, 49, e2022GL098158. doi.org: 10.1029/2022GL098158
- 362 Ward, S. (2002). Tsunamis, *Encyclopedia of Physical Science and Technology* Vol. 17. ed. Meyers,
363 RA, Academic Press, San Diego, 175-191.
- 364 Wessel, P. (2009). Analysis of Observed and Predicted Tsunami Travel Times for the Pacific and
365 Indian Oceans. *Pure and Applied Geophysics*, 166(1–2), 301–324.
366 <https://doi.org/10.1007/s00024-008-0437-2>
- 367 Wright, C.J., et al. (2022) Tonga eruption triggered waves propagating globally from surface to edge
368 of space, *ESSOAr*, <https://www.essoar.org/pdfjs/10.1002/essoar.10510674.1>
- 369 Zedek, F., Rolland, L. M., Mikesell, T. D., Sladen, A., Delouis, B., Twardzik, C., & Coïsson, P. (2021).
370 Locating surface deformation induced by earthquakes using GPS, GLONASS and Galileo
371 ionospheric sounding from a single station. *Advances in Space Research*, 68(8), 3403–3416.
372 <https://doi.org/10.1016/j.asr.2021.06.011>

373

374

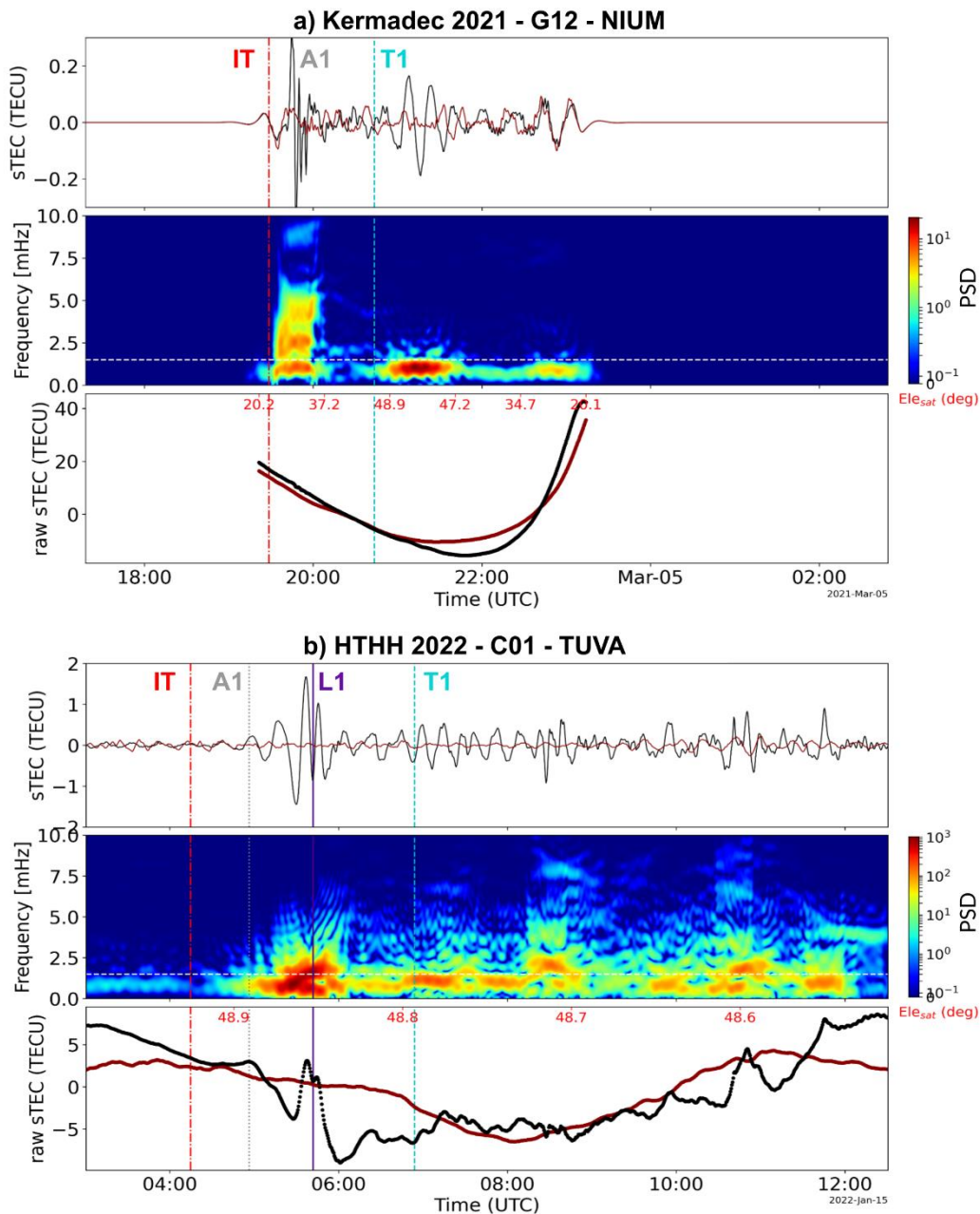
375 **Figure Captions**

376



377
 378
 379
 380
 381
 382
 383
 384
 385
 386
 387

Figure 1. (a) Context map of the study with locations of the tsunami sources and measurements. The Jan. 15, 2022, Hunga Tonga-Hunga Ha’apai volcanic eruption and the Mar. 4, 2021, 8.1 Mw Kermadec Islands earthquake epicenter are marked with a blue and purple star, respectively. GNSS receivers are marked with triangles of the same color. The contours highlight the Hunga theoretical tsunami traveling times (TTT). Ionospheric Pierce Points (IPPs at 300km altitude) are depicted by colored dots for the selected pairs, while gray dots represent that of other pairs. **(b)** A selection of filtered sTEC measurements with tsunami-induced signature. Satellites are marked with a letter: Beidou (C), QZSS (J), GPS (G), GLONASS (R), Galileo (E), and PRN number. To highlight the tsunami signature, the time series are aligned with respect to the tsunami theoretical arrival time (TTT).



388

389

390

391

392

393

394

395

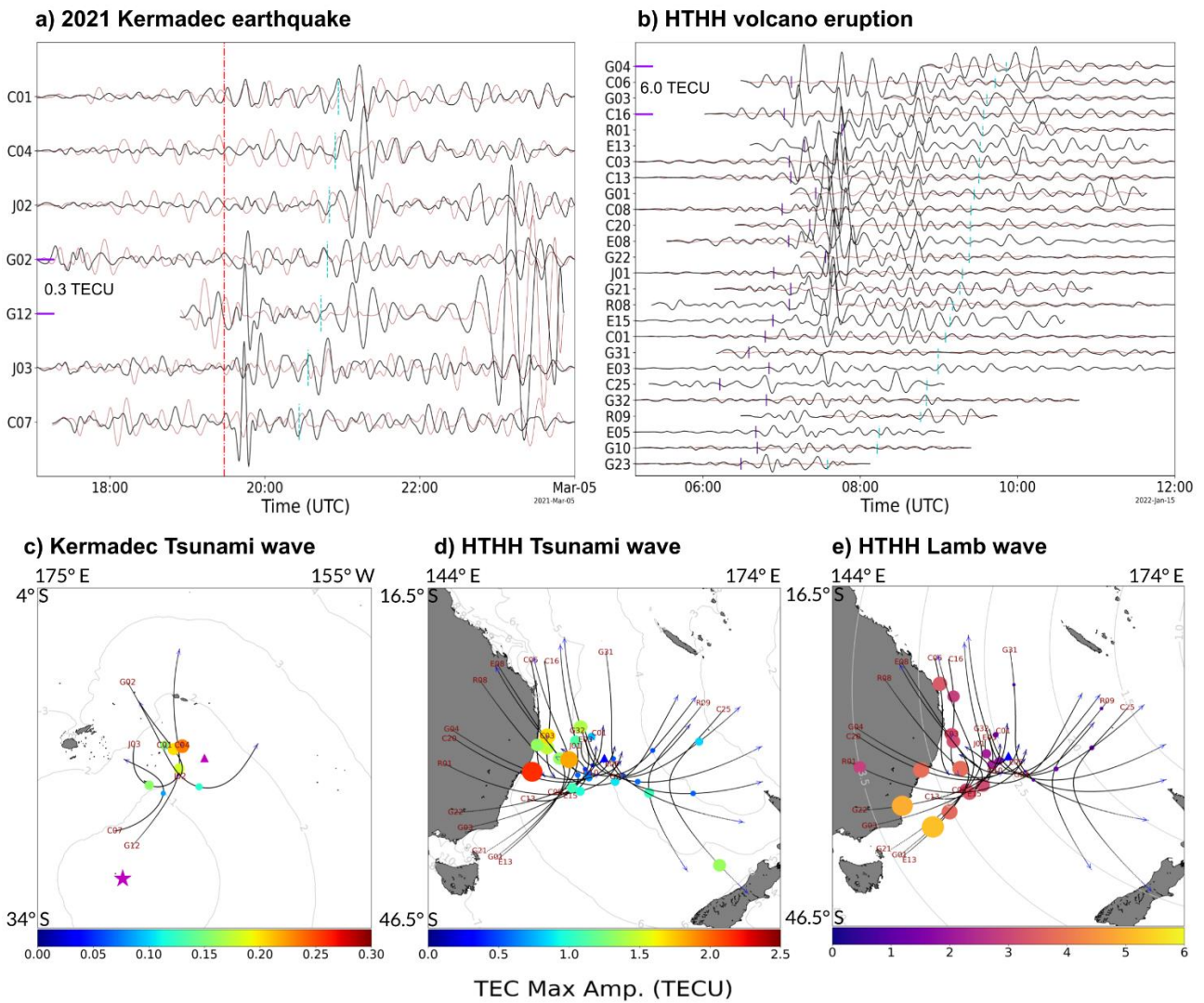
396

397

398

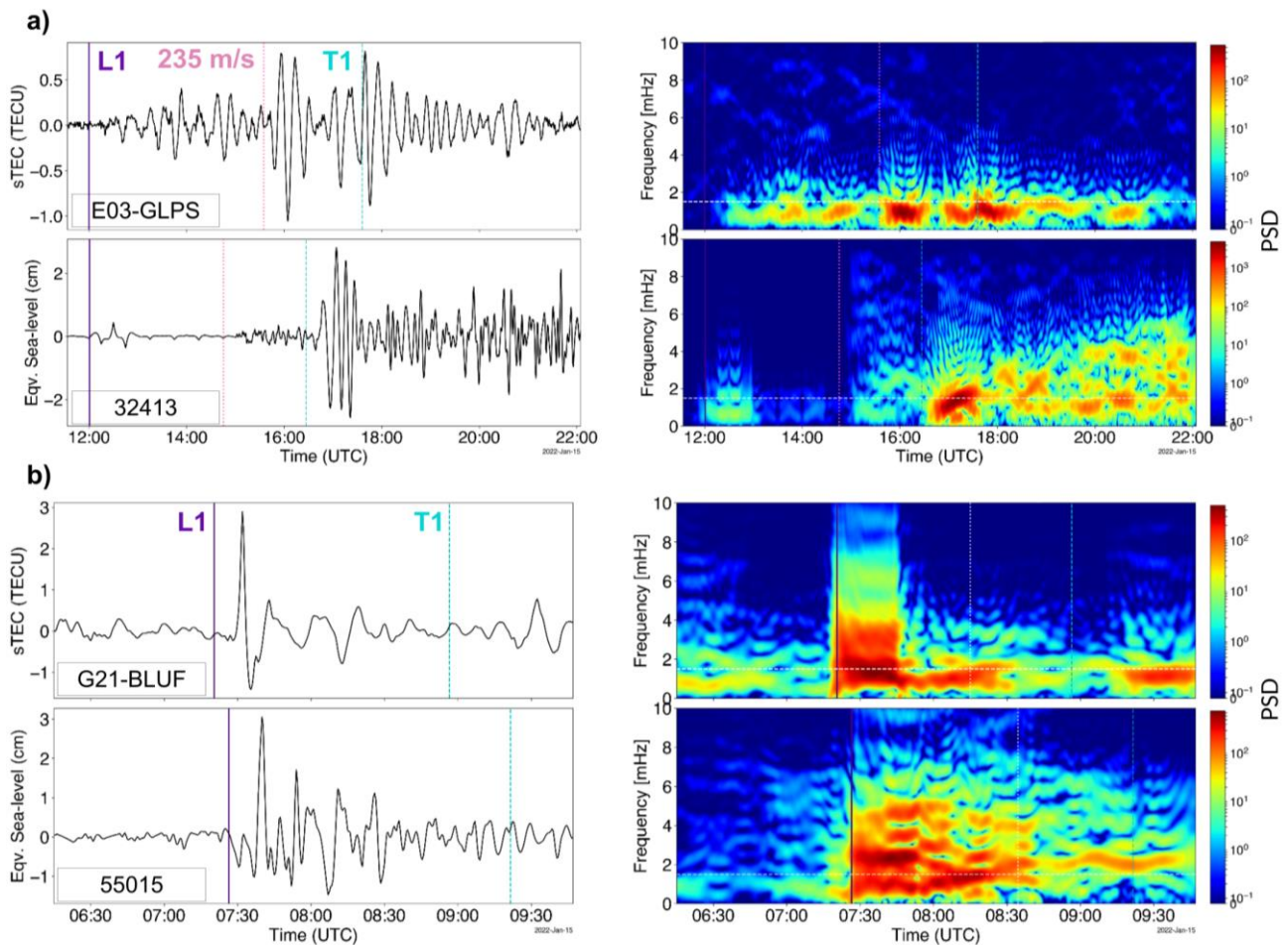
399

Figure 2. Comparison between the ionospheric TEC imprints obtained by the satellite-receiver pairs G12-NIUM (Kermadec) and C01-TUVA (HTHH). **(a)** TEC measurements during the Kermadec earthquake and the passage of the triggered tsunami. The three panels from bottom to top are: the raw sTEC, the event day filtered sTEC spectrogram, and the filtered sTEC. The filtered sTEC is zero-padded to match the length of C01-TUVA. The vertical red line represents the event initiation time (IT). The top x-axes show the satellite's azimuth and elevation, respectively. The horizontal white line in the spectrogram indicates the expected frequency of tsunami ionospheric signature (i.e., 1.5mHz; 11min). **(b)** TEC measurements during the HTHH volcanic eruption and the produced tsunami passage. The expected arrival times of the acoustic pulse A1; 667m/s, the Lamb wave L1; 318m/s and the tsunami are highlighted.



400
 401 **Figure 3. (a)** The tsunami-induced ionospheric signatures detected in the vicinity of Niue Island
 402 (NIUM) after the 2021 Kermadec earthquake. **(b)** The ionospheric imprints detected in the vicinity
 403 of Lord Howe Island (LORD) induced after the HTHH volcanic eruption. **(c)** Geographic view of the
 404 earthquake's epicenter, the GNSS receiver, and the ionospheric tracks of the satellites whose sTEC
 405 time series are shown in (a). Along the satellites' tracks, the disks indicate the satellites' locations at
 406 the tsunami expected arrival time, whose size and color point out the detected maximum sTEC
 407 amplitude of the tsunami imprints. The max sTEC amplitude is calculated within a 2-hour
 408 observation window starting 15 minutes before TAT as $\frac{max_{obs.w} - min_{obs.w}}{2}$. **(d)** Map showing the GNSS
 409 receiver and the ionospheric tracks of the satellites whose sTEC time series are shown in (b). **(e)** The
 410 disks depicted in the map show the satellites' locations at the Lamb wave arrival, with their size and
 411 color representing the wave's maximum sTEC amplitude. The results illustrated by (c), (d), and (e)
 412 demonstrate that ionospheric imprints downstream of the receiver display larger max sTEC amp.
 413 than upstream, as expected from IGWs.

414
 415
 416



417

418 **Figure 4.** Comparison between open-ocean sea-level anomaly and ionospheric signatures in the
 419 vicinity of Galapagos Islands (a) and southern New Zealand (b) on Jan. 15, 2022. Time series are on
 420 the left, and spectrograms are on the right. **(a)** The top panel shows the filtered E03-GLPS sTEC
 421 measurements. The bottom panel presents the sea-level measurements from the tsunami buoy
 422 DART 32413. **(b)** The top panel is the sTEC measurements of G21-BLUF, and the bottom is the sea-
 423 level observation of DART 55015. The results show that the Lamb wave is better sensed in the
 424 vicinity of southern New Zealand, whereas near the Galapagos Islands, the tsunami is. In addition,
 425 the comparison presents a solid confirmation of the origin of each imprint.